frontiers | Frontiers in Earth Science

ORIGINAL RESEARCH
published: 24 June 2022
doi: 10.3389/feart.2022.897396

Increased Terrigenous Supply to the Pelagic Panthalassa Superocean Across the Carnian Pluvial Episode: A Possible Link With Extensive Aridification in the Pangean Interior

Tenichi Cho[1]*, *Masayuki Ikeda*[2] and *Tohru Ohta*[3]

[1]Graduate School of Creative Science and Engineering, Waseda University, Shinjuku, Japan, [2]Department of Earth and Planetary Science, The University of Tokyo, Bunkyo, Japan, [3]Department of Earth and Sciences, Faculty of Education and Integrated Arts and Sciences, Waseda University, Shinjuku, Japan

OPEN ACCESS

Edited by:
Jacopo Dal Corso,
China University of Geosciences
Wuhan, China

Reviewed by:
Or M. Bialik,
University of Malta, Malta
Paul Wignall,
University of Leeds, United Kingdom

***Correspondence:**
Tenichi Cho
tianct@fuji.waseda.jp

Specialty section:
This article was submitted to Sedimentology, Stratigraphy and Diagenesis, a section of the journal Frontiers in Earth Science

Received: 16 March 2022
Accepted: 16 May 2022
Published: 24 June 2022

Citation:
Cho T, Ikeda M and Ohta T (2022) Increased Terrigenous Supply to the Pelagic Panthalassa Superocean Across the Carnian Pluvial Episode: A Possible Link With Extensive Aridification in the Pangean Interior. Front. Earth Sci. 10:897396. doi: 10.3389/feart.2022.897396

In the Late Triassic, a global environmental change called the Carnian Pluvial Episode (CPE) emerged, causing major biological turnover. The CPE has been recognized by siliciclastic input to sedimentary basins, multiple carbon isotope perturbations, and climate proxies for humidification. The CPE is considered to have been associated with increased atmospheric pCO_2 from eruptions of large igneous provinces. However, the nature of this global environmental perturbation on the continents is still not well understood. Here we present a geochemical analysis of a pelagic deep-sea bedded chert sequence across the CPE in the Jurassic accretionary complex of Mino terrane, central Japan. Fluctuations in terrigenous material supply were reconstructed using Principal Component Analysis of major element compositions. The first principal component positively correlates with elements enriched in clay minerals such as Al_2O_3, whereas it negatively correlates with CaO, P_2O_5, and MnO, derived from apatite and manganese. A sudden increase in terrigenous supply was detected around the Julian/Tuvalian boundary, suggesting that CPE-related siliciclastic input also occurred in the abyssal plain environment. The terrigenous supply returned to the pre-CPE state in the Tuvalian. Since the terrigenous material supplied to the abyssal plain is thought to be derived from eolian dust blown from continental arid regions, the increasing terrigenous supply detected in the pelagic deep-sea chert succession may indicate extensive aridification. This result seems to conflict with the common view of the CPE as a humidification event. This contradiction possibly suggests that the extensive aridification occurred within the interior of the supercontinent Pangea, while hydrological circulation enhanced on the coastal region during the CPE.

Keywords: CPE, bedded chert, eolian dust, abyssal plain, pangea, panthalassa, compositional data analysis, major element

1 INTRODUCTION

1.1 Carnian Pluvial Episode

The Carnian Pluvial Episode (CPE) was a time of global environmental perturbations with significant biological turnover both in the ocean and on land (e.g., Simms and Ruffell, 1989; Dal Corso et al., 2020). The CPE was initially recognized in many European sedimentary basins as drastic lithologic changes, such as the demise of carbonate platforms and increased siliciclastic input (e.g., Gattolin et al., 2015). Multiple negative shifts of $\delta^{13}C$ are recognized across the CPE, suggesting a link with volcanic activity of Wrangellia LIPs (e.g., Dal Corso et al., 2018). Recent studies revealed that the intensification of the hydrological cycle also occurred not only in the western Tethys realm but in worldwide sedimentary basins (e.g., North China Plate; Lu et al., 2021; Boreal realm; Mueller et al., 2016; Gondwana region; Bernardi et al., 2018).

In contrast, the terrestrial records of the Pangean inland region are still controversial. Paleoclimate proxies, such as clay mineral profiles and paleosols, suggest only minor climate change with a generally arid to semi-arid background climate across the CPE from the United Kingdom (Baranyi et al., 2019a) and from Spain (Barrenechea et al., 2018), while data from the Germanic Basin and the Danish Basin did not show any humidity signal across the CPE (Visscher et al., 1994; Lindström et al., 2017). Enhanced continental weathering related to a more humid climate is only suggested for the early stages of the CPE in the Julian 2 (Baranyi et al., 2019b). Such observed discrepancies in the environmental signal across the CPE seem to be related to the contrasts in the

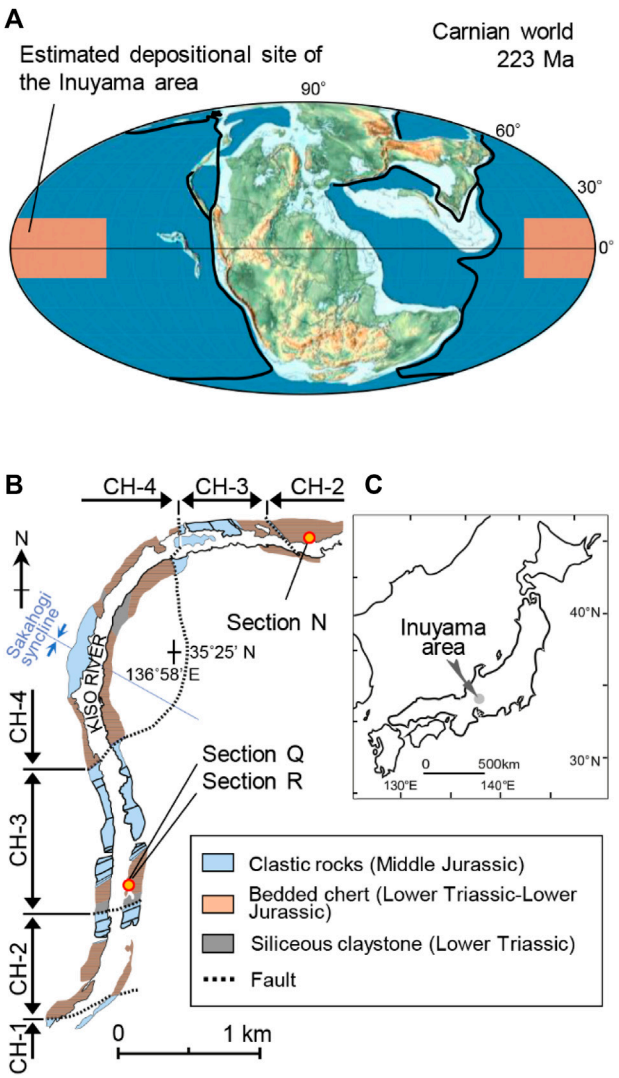

FIGURE 1 | (A) Carnian paleogeography (modified after Scotese, 2014). The shaded region shows a possible area within which the Inuyama succession was likely deposited. Subduction zones are shown in black lines (from Matthews et al., 2016) **(B)** Geologic map and **(C)** location map showing the location of the Carnian bedded chert successions in Inuyama area, central Japan (modified after Kimura and Hori, 1993).

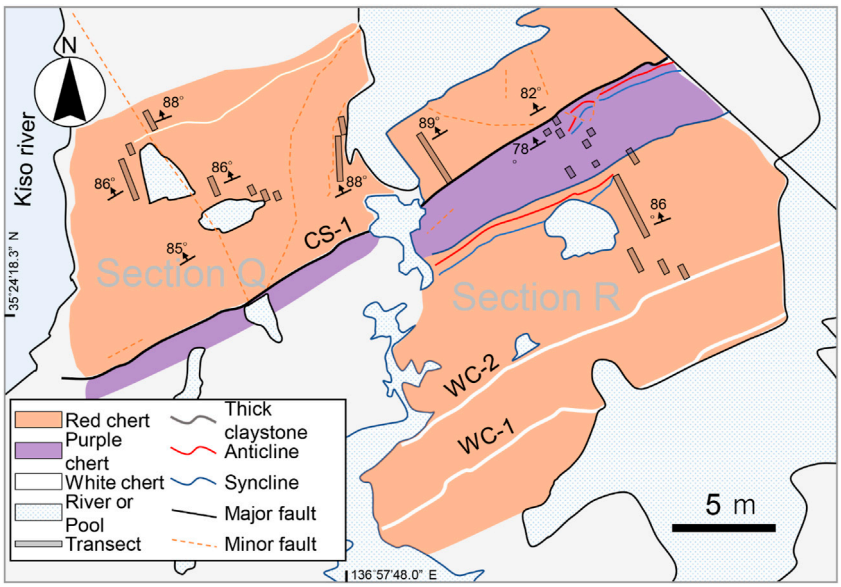

FIGURE 2 | Detailed geologic map of Section R and Section Q of Sugiyama (1997). Continuous composite lithostratigraphy was described in grey lines.

climate of different regions and the limited age constraint of the terrestrial strata.

Abyssal deep-sea sediment provides a relatively continuous and consistent archive (e.g., Ikeda and Tada., 2014). An increase in the relative abundance of smectite among Fe-bearing minerals was detected in Japanese pelagic deep-sea chert across Julian/Tuvalian boundary (Nakada et al., 2014). Studies of Cenozoic sediments show that the terrigenous materials supplied to abyssal plains are mostly eolian dust generated from continental arid regions (e.g., Asahara, 1999). It is also noteworthy that a relatively thick, muddy silicious claystone interval (CS-1; Sugiyama, 1997) is observed within the smectite interval (Nakada et al., 2014). Along with the presence of CS-1, the thickness of intercalated mudstones drastically increased above the CS-1, and this can be correlated at least regionally (Sugiyama, 1997; Sugiyama et al., 2001). Because chert mainly consists of radiolarian tests and eolian mudstone (e.g., Hori et al., 1993), such an increase in mudstone may be related to increased eolian supply and/or decreased productivity (Sugiyama, 1997). The paleoenvironmental significance of these lithologic changes in the Carnian bedded cherts remains unclear.

In this study, the Carnian bedded cherts from the type section of Japanese radiolarian zones were investigated in order to elucidate the influence of the CPE on the Pangean interior. We seek to extract terrestrial environmental conditions by investigating the geochemistry of the intercalated mudstone of the bedded cherts, which concentrate terrigenous materials much higher than chert layers. The terrigenous content fluctuation was reconstructed throughout the Carnian by multivariate statistical analyses of major element composition. The increase of terrigenous materials flux implying reinforcement of eolian supply occurred. Our results thus firstly provide evidence that extensive aridification occurred in the inland of the Pangea across the CPE.

2 GEOLOGICAL SETTING AND LITHOLOGY DESCRIPTION

2.1 Geological Background

Early Triassic to Early Jurassic bedded chert is exposed in the Inuyama area, central Japan, as a part of the Mino-Tamba belt, Jurassic accretionary complex (**Figure 1**). The bedded cherts and the overlying Middle Jurassic clastic rocks are repeatedly exposed as a chert-clastic sequence truncated by bedding-parallel thrusts (**Figure 1B**; Yao et al., 1980; Matsuda and Isozaki, 1991). Since this bedded chert had an extremely slow sedimentation rate of 1–3 mm/kyr, and lacks coarse-grained terrigenous material for over 60 Myr, it is considered to have been deposited in a distal setting (Matsuda and Isozaki, 1991; Hori et al., 1993). The latitude of the depositional site was estimated as 12.3° ± 5.6°N or S and 19.0° ± 10.5°N or S for 237 Ma and 223.5 Ma, respectively based on the inclination of magnetic component of hematite (**Figure 1A**; Oda and Suzuki, 2000).

Bedded cherts are composed of rhythmic alteration of chert layers (cm scale) and intercalated mudstones. Chert layers are mainly composed of microcrystalline quartz and biogenic siliceous tests, whereas intercalated mudstones are mainly composed of clay minerals derived from eolian dust brown from the continental region (Hori et al., 1993). The relationship of chemical composition of chert layers and intercalated mudstones has been recognized as silica dilution by radiolarian test through the observation of negative correlation of SiO2 with other elements (e.g., Hori et al., 2000).

Bedded cherts are considered to be formed by a diagenetic segregation process as silica dissolution and transportation (Tada, 1991). The lithology of bedded cherts in the Inuyama area is mainly divided into two types: F type and B type which denote “fine grained quartz” and “biogenic clasts”, respectively (Imoto 1983; Sugiyama, 1997). F-type cherts show a few siliceous biogenic tests scattered in

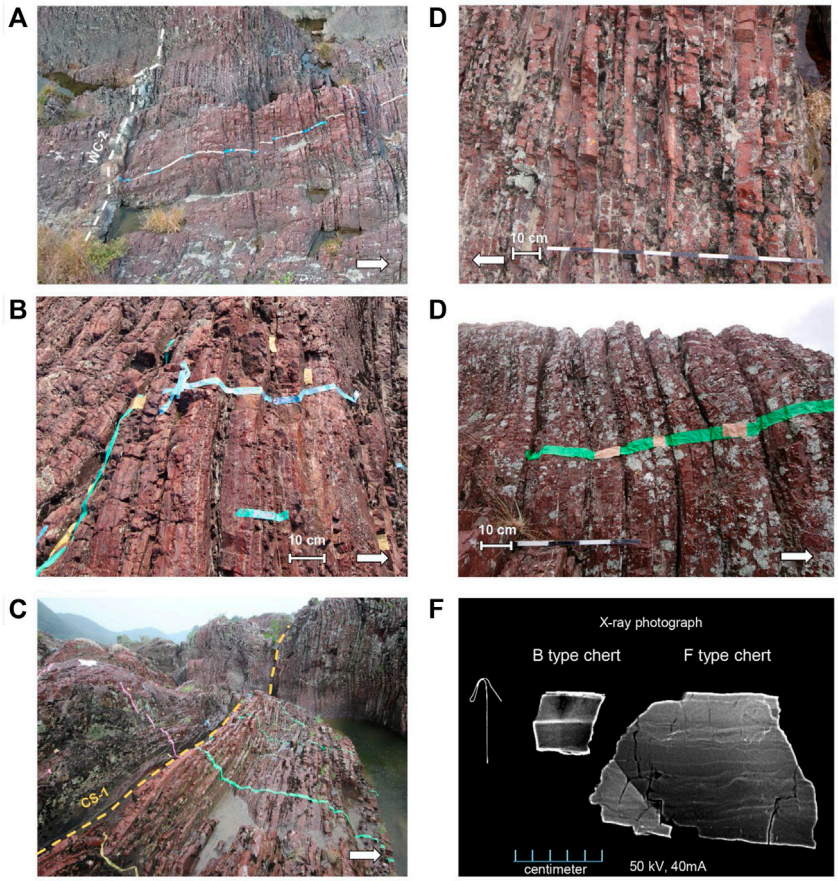

FIGURE 3 | Representative outcrop photographs of the Carnian bedded cherts **(A)** White chert WC-2 and Julian F-type red chert. The boundary of red and purple chert can be seen on the right side of the photograph. **(B)** Close-up of Julian F-type purple chert. Millimeter to cm scale lamination and bedding is observed as changes in color and silica content **(C)** Thick claystone layer CS-1 located at the boundary of F-type purple chert and B-type red chert. **(D)** Close-up of the B-type red chert (Julian-Tuvalian) with relatively thick intercalated mudstones. **(E)** Close-up of the F-type red chert (Tuvalian). The Intercalated mudstones of the F-type cherts are very thin (<5 mm). **(F)** Soft X-ray photograph of B-type (Julian-Tuvalian) and F-type (Tuvalian) chert. Thick intercalated mudstones are observed on the B-type chert whereas millimeter scale lamination can be seen on the F-type chert. Tape width in **(A,C,E)** is 5 cm. Scale bars are 10 cm. The white arrows indicate way-up.

the fine-grained quartz matrix under microscopic observation with very thin (*ca.* 0.5–2 mm) intercalated mudstone layers and laminations. B-type cherts show concentrated biogenic tests under microscopic observation and are usually associated with thick (*ca.* 2–20 mm) intercalated mudstones. The difference in their formation mechanism may be related to changes in silica and terrigenous contents of the precursor sediment of bedded chert, formed by cyclic changes of sedimentary environments and/or diagenetic conditions (Sugiyama, 1997).

In this study, Section R and Section Q of Sugiyama (1997) in the Inuyama area are selected for detailed geological mapping and geochemical study in order to reconstruct paleoclimatic conditions of the entire Carnian stage (**Figures 1**, **2**). Section R is the type section of Japanese radiolarian zone TR5A, which contains the most complete and unaltered sequence of the TR5A zone (Sugiyama, 1997). Section Q is located to the west of Section R and is one of the most complete and unaltered sequences of TR5B zone in Inuyama area (Sugiyama, 1997).

The depositional age of the Carnian bedded chert is constrained by radiolarian and conodont biostratigraphy, cyclostratigraphy, and carbon isotope stratigraphy (Sugiyama, 1997; Ikeda and Tada., 2014; Nakada et al., 2014; Yamashita et al., 2018; Tomimatsu et al., 2021). Sugiyama (1997) correlated interval (*ca.* 20 m thick) from the upper part of the radiolarian zone TR4B (*Spongoserrula delhi*) to the lower part of TR6A (*Capnodoce–Trialatus*) based on the first occurrence (FO) of the Carnian radiolaria *Praeheliostaurus laevis*, the FO of Carnian conodont *Neogondolella foliata*, and the FO of Norian radiolaria *Capnodoce gilis* in Sections N, R and Q in Inuyama area. Nakada et al. (2014) assigned the Julian/Tuvalian boundary within the *Elbistanium gracile* radiolarian zone between their samples R3-1 and R5-3. Tomimatsu et al. (2021) detected two negative excursions in carbon isotopes, NCIE-α and NCIE-β, in

TABLE 1 | Major element composition of bedded chert samples collected in this study.

	Height	Lithology	Color	SiO2	TiO2	Al2O3	Fe2O3	MnO	MgO	CaO	Na2O	K2O	P2O5	LOI_{550}	LOI_{950}
sample	(mm)			(wt%)	(wt%)	(wt%)	(wt%)	(wt%)	(wt%)	(wt%)	(wt%)	(wt%)	(wt%)	(wt%)	(wt%)
WC2	0	Intercalated mudrock	red	56.04	1.61	21.91	8.68	0.470	3.94	0.92	0.24	5.07	0.525	3.36	1.77
Ra3.9	841	Intercalated mudrock	red	61.39	1.34	17.21	8.84	1.243	3.41	0.67	0.19	4.46	0.338	3.85	1.61
Ra4	875	Intercalated mudrock	red	55.78	1.16	19.82	10.87	0.408	5.00	0.59	0.19	4.80	0.253	4.33	1.60
Ra8.2	1,594	Intercalated mudrock	red	55.49	1.07	18.43	12.07	0.665	7.06	0.49	0.14	3.68	0.254	5.27	1.38
Ra9.9	2,273	Intercalated mudrock	red	49.05	2.27	22.66	11.04	0.346	3.97	1.75	0.24	6.52	1.142	4.14	1.82
Ra12	3,122	Intercalated mudrock	red	55.82	1.79	19.63	9.61	0.201	3.61	0.84	0.24	6.16	0.558	3.95	1.36
Ra14	3,540	Intercalated mudrock	red	54.79	1.33	19.63	10.00	0.160	3.84	1.32	0.24	6.37	0.773	4.01	1.60
Ra16	4,019	Intercalated mudrock	red	59.27	1.33	17.83	9.66	0.158	3.31	0.65	0.22	5.73	0.367	3.59	1.51
Ra18	4,511	Intercalated mudrock	red	54.71	1.10	19.16	10.85	0.184	5.47	0.82	0.19	5.61	0.374	4.42	1.63
Ra18.2	4,630	Intercalated mudrock	red	52.97	1.36	20.34	12.08	0.180	4.90	1.10	0.28	5.51	0.595	4.36	2.39
Ra20	4,975	Intercalated mudrock	red	57.37	1.04	18.13	10.43	0.230	5.51	0.69	0.16	5.24	0.273	3.78	1.91
Ra22	5,342	Intercalated mudrock	red	71.54	0.92	12.68	6.98	0.126	2.05	0.36	0.20	4.02	0.170	3.05	1.51
Ra24	5,532	Intercalated mudrock	red	65.58	1.11	15.64	7.57	0.329	2.61	0.36	0.21	5.22	0.157	2.82	1.59
Ra26	5,956	Intercalated mudrock	purple	58.56	1.15	18.89	8.42	0.255	4.06	0.70	0.22	5.99	0.311	3.44	2.07
Ra28	6,774	Intercalated mudrock	purple	62.06	1.25	16.95	8.26	0.170	3.37	0.59	0.21	5.61	0.328	3.14	1.89
Ra30	7,276	Intercalated mudrock	purple	55.63	1.05	19.67	8.90	0.467	5.90	0.70	0.20	5.62	0.278	4.31	2.14
Ra33.9	7,404	Intercalated mudrock	purple	67.83	1.40	15.03	6.96	0.219	2.97	0.44	0.22	4.05	0.187	3.04	1.70
Ra32	7,790	Intercalated mudrock	purple	65.72	0.90	16.40	5.81	0.098	3.06	0.58	0.20	5.48	0.235	3.45	1.76
Ra35.9	7,893	Intercalated mudrock	purple	55.32	1.38	20.33	8.83	0.176	3.50	1.09	0.20	6.99	0.649	3.20	1.95
Ra36	7,999	Intercalated mudrock	purple	67.16	1.14	14.06	8.18	0.142	2.75	0.58	0.17	4.54	0.336	2.70	1.87
Ra37	8,117	Intercalated mudrock	purple	67.25	1.17	14.66	7.99	0.097	2.43	0.66	0.20	4.79	0.321	2.77	1.79
Ra39-1	8,839	Intercalated mudrock	purple	63.87	0.83	14.60	6.53	0.134	2.62	4.35	0.28	4.27	2.768	3.43	2.10
Ra39-2	8,840	Intercalated mudrock	purple	47.25	0.87	17.61	4.88	0.085	3.10	11.12	0.27	6.27	7.475	2.70	2.41
Ra40	8,865	Intercalated mudrock	purple	60.18	0.97	15.51	7.52	0.189	2.91	3.72	0.25	5.50	2.391	2.90	2.19
CS1	9,024	Intercalated mudrock	red	63.8	0.91	16.23	8.02	0.146	3.30	0.35	0.22	5.65	0.095	3.36	1.38
R1	9,053	Intercalated mudrock	red	59.52	1.05	17.44	10.98	0.360	4.29	0.32	0.15	4.90	0.122	3.05	1.54
R4	9,137	Intercalated mudrock	red	58.25	1.25	19.13	9.44	0.185	3.77	0.41	0.23	5.97	0.127	3.85	2.10
R8	9,369	Intercalated mudrock	red	55.62	1.17	19.51	11.02	0.274	5.14	0.40	0.20	5.41	0.117	4.03	2.28
R9	9,383	Intercalated mudrock	red	54.12	1.40	20.18	11.14	0.281	4.61	0.48	0.22	6.18	0.158	3.54	2.04
R10	9,426	Intercalated mudrock	red	51.06	1.22	20.22	12.89	0.443	8.10	0.60	0.14	3.90	0.151	4.82	2.44
R13	9,545	Intercalated mudrock	red	53.31	1.61	20.93	11.51	0.449	4.66	0.47	0.23	5.74	0.163	3.90	2.21
R15	9,610	Intercalated mudrock	red	60.72	1.02	17.72	9.66	0.210	3.89	0.45	0.17	4.95	0.180	3.03	1.56
R16	9,642	Intercalated mudrock	red	75.31	0.59	11.59	5.41	0.163	2.01	0.21	0.11	3.72	0.073	1.77	1.17
R19	9,678	Intercalated mudrock	red	61.85	1.41	17.39	10.66	0.220	2.83	0.41	0.18	5.35	0.286	2.72	1.86
R22	9,778	Intercalated mudrock	red	69.69	0.73	14.13	6.66	0.229	2.61	0.34	0.13	4.67	0.161	2.20	1.30
R23	9,791	Intercalated mudrock	red	64.33	1.05	15.70	9.15	0.329	3.28	0.37	0.14	4.78	0.182	2.86	1.58
R24	9,824	Intercalated mudrock	red	64.44	0.85	15.51	9.36	0.325	3.11	0.40	0.13	5.17	0.181	2.44	1.51
R25	9,866	Intercalated mudrock	red	64.82	0.99	15.44	8.92	0.292	2.76	0.39	0.15	5.11	0.177	2.20	1.44
R26	9,917	Intercalated mudrock	red	57.14	1.14	19.82	10.26	0.478	3.65	0.46	0.20	6.41	0.213	2.85	1.62
R27	9,925	Intercalated mudrock	red	61.71	1.15	16.59	10.43	0.371	5.09	0.39	0.10	3.98	0.178	3.31	1.53
R28	9,952	Intercalated mudrock	red	57.70	0.99	19.52	9.42	0.290	3.74	0.46	0.18	6.30	0.188	3.01	1.80
R29	9,980	Intercalated mudrock	red	61.34	0.92	18.63	8.55	0.243	3.54	0.34	0.17	6.16	0.137	2.60	1.84
R30	10,012	Intercalated mudrock	red	61.43	0.96	18.29	8.98	0.272	3.26	0.35	0.18	5.87	0.151	2.64	1.44
R31	10,080	Intercalated mudrock	red	61.41	1.00	19.26	9.37	0.185	3.55	0.39	0.19	6.18	0.126	2.67	1.70
R32	10,121	Intercalated mudrock	red	54.39	1.15	21.13	10.44	0.192	4.06	0.59	0.22	6.82	0.280	2.98	1.84
R36	10,179	Intercalated mudrock	red	54.77	1.03	20.74	9.69	0.367	4.11	0.63	0.18	6.98	0.287	3.16	1.99
R37	10,189	Intercalated mudrock	red	58.08	1.03	18.26	9.80	0.257	3.57	0.91	0.16	6.35	0.505	2.71	1.82
R38	10,217	Intercalated mudrock	red	56.16	1.10	19.43	9.80	0.463	4.85	0.63	0.16	6.01	0.281	3.22	1.93
R39	10,255	Intercalated mudrock	red	55.61	1.14	19.35	10.55	0.334	4.88	0.69	0.18	5.82	0.326	3.12	2.08
R40	10,325	Intercalated mudrock	red	57.33	0.96	18.68	10.49	0.311	4.04	0.51	0.17	6.30	0.225	2.91	1.81
R41	10,354	Intercalated mudrock	red	61.12	1.00	19.88	9.42	0.262	4.17	0.48	0.18	6.34	0.210	2.74	1.88
R42	10,390	Intercalated mudrock	red	58.50	0.95	19.15	9.86	0.309	4.42	0.72	0.16	6.04	0.352	2.86	1.95
R44	10,421	Intercalated mudrock	red	63.28	0.91	17.19	8.58	0.267	3.98	0.44	0.16	5.59	0.183	2.54	1.74
R45	10,449	Intercalated mudrock	red	65.36	0.89	15.44	8.88	0.357	4.21	0.50	0.13	4.63	0.236	2.59	1.52
R46	10,481	Intercalated mudrock	red	78.00	0.58	9.20	6.87	0.501	2.16	0.31	0.09	2.70	0.141	2.18	1.36
R47	10,508	Intercalated mudrock	red	60.80	1.04	17.66	10.31	0.329	3.90	0.48	0.13	5.46	0.218	2.59	1.73
R49	10,567	Intercalated mudrock	red	62.91	0.93	17.27	9.09	0.302	3.51	0.69	0.14	5.42	0.349	2.54	1.72
R50	10,587	Intercalated mudrock	red	67.84	0.88	13.36	9.85	0.622	2.78	0.45	0.12	4.27	0.227	2.41	1.57
R51	10,605	Intercalated mudrock	red	63.81	0.98	16.15	9.55	0.446	3.46	0.68	0.14	4.88	0.361	2.43	1.58
R52	10,641	Intercalated mudrock	red	63.34	0.89	16.19	9.85	0.495	3.76	0.60	0.14	4.85	0.296	2.45	1.72
R53	10,670	Intercalated mudrock	red	76.63	0.57	10.34	6.34	0.439	2.50	0.39	0.10	3.03	0.184	1.68	1.22
R54	10,689	Intercalated mudrock	red	59.55	0.99	17.85	10.92	0.503	4.04	0.59	0.15	5.35	0.288	2.80	1.75
R55	10,714	Intercalated mudrock	red	60.42	1.05	17.57	10.44	0.575	3.65	0.55	0.15	5.39	0.251	2.72	1.68

(Continued on following page)

TABLE 1 | (*Continued*) Major element composition of bedded chert samples collected in this study.

	Height	Lithology	Color	SiO2	TiO2	Al2O3	Fe2O3	MnO	MgO	CaO	Na2O	K2O	P2O5	LOI_{550}	LOI_{950}
R56	10,742	Intercalated mudrock	red	67.34	0.95	14.08	8.95	0.732	3.19	0.51	0.13	4.10	0.248	2.48	1.40
R59	10,817	Intercalated mudrock	red	72.54	0.8	10.98	8.51	0.937	2.93	0.40	0.10	3.02	0.187	2.16	1.11
R64	10,885	Intercalated mudrock	red	48.64	1.31	19.08	13.75	4.624	5.78	0.94	0.20	4.68	0.349	4.48	2.57
R81	11,021	Intercalated mudrock	red	61.28	1.19	15.02	10.96	0.707	3.61	0.77	0.19	4.68	0.422	2.97	1.71
R82	11,032	Intercalated mudrock	red	58.11	1.25	16.94	11.48	0.541	3.39	0.75	0.22	5.55	0.388	3.11	1.98
R84	11,049	Intercalated mudrock	red	52.80	1.4	20.14	12.24	0.934	4.08	0.82	0.24	5.56	0.395	3.47	2.07
R85	11,085	Intercalated mudrock	red	49.64	1.63	20.03	14.82	0.996	3.94	1.17	0.25	5.65	0.656	3.48	2.04
Q-2	11,954	Intercalated mudrock	red	51.05	2.08	22.46	12.16	0.422	3.20	0.26	0.31	6.10	0.212	3.70	2.13
Q-1	12,255	Intercalated mudrock	red	52.67	1.48	19.81	13.95	0.717	3.98	0.66	0.23	5.15	0.350	3.17	1.84
Q0	13,008	Intercalated mudrock	red	55.88	1.1	18.99	10.36	0.403	3.76	0.83	0.23	6.54	0.506	4.08	1.63
Q1	13,112	Intercalated mudrock	red	50.97	1.46	21.51	12.58	0.694	4.50	0.55	0.28	5.86	0.271	3.59	2.17
Q2	13,924	Intercalated mudrock	red	59.43	1.35	16.31	12.66	0.689	3.98	0.44	0.20	4.10	0.230	3.52	2.03
Q3	14,301	Intercalated mudrock	red	70.16	1.17	11.91	9.12	0.363	2.37	0.66	0.17	3.29	0.373	1.48	1.49
Q4	14,865	Intercalated mudrock	red	50.73	1.8	20.64	14.17	0.672	3.92	0.55	0.26	5.50	0.382	4.12	2.18
Q5	15,411	Intercalated mudrock	red	58.52	1.76	14.83	13.78	2.134	2.93	0.66	0.19	3.98	0.427	3.66	1.89
Q6	15,839	Intercalated mudrock	red	52.78	1.53	19.41	13.66	2.819	3.73	0.50	0.23	4.69	0.233	4.37	2.32
Q7	16,525	Intercalated mudrock	red	80.79	0.78	7.96	5.33	0.670	1.88	0.32	0.11	1.87	0.135	0.77	1.08
Q7.9	17,382	Intercalated mudrock	red	52.02	1.33	21.84	11.90	0.516	3.96	0.52	0.20	6.12	0.339	4.02	2.06
Q10	18,464	Intercalated mudrock	red	56.34	1.46	17.86	11.24	1.315	3.26	0.48	0.22	5.97	0.302	3.95	1.64

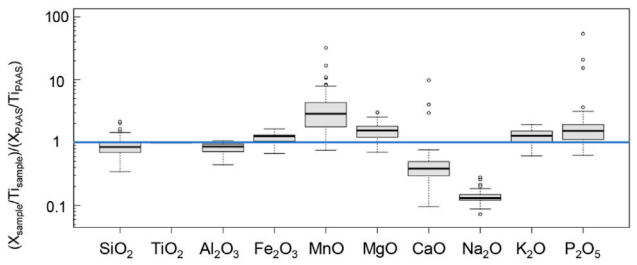

FIGURE 4 | PAAS (Post-Archean Australian Shale)-normalized elemental abundance of the intercalated mudstone of the bedded chert from Section R and Section Q. Boxes indicate the 25th and 75th percentiles. The horizontal line in each box marks the median value. Whiskers represent the 1.5 times the interquartile range of the data. Open circles represent data outliers. Note that the vertical axis is a logarithmic scale. PAAS data are from Taylor and McLennan (1985).

the TR5A zone within the *Nicoraella*? *budaensis* conodont zone in Section N, and correlated them to the global carbon isotopic excursion across the CPE.

2.2 Field Description

We conducted a detailed three-dimensional outcrop observation and constructed a bed-by-bed scale continuous lithostratigraphy to avoid missing or duplicating the strata (**Figure 3**). The lithological column was made from the lower part of Section R to the upper part of Section Q, in ascending order. The F-type red chert is dominant with a white chert bed WC-2 of Sugiyama (1997) at the base. About 900 cm above WC-2, the chert changes to *ca.* 300 cm purple laminated interval. Above the purple chert interval, *ca.* 200 cm B-type chert is intercalated with the *ca.* 20 cm siliceous claystone bed CS-1 of Sugiyama (1997) at the base. The CS-1 between F-type chert to B-type chert is widely recognized, not only in Inuyama area, but also in Hisuikyo area, which is 25 km north to Inuyama area (Sugiyama, 1997; Sugiyama et al., 2001).

3 MATERIALS AND METHODS

3.1 Geochemical Analysis

Eighty-one intercalated mudstone samples were collected from Sections R and Q to cover the Carnian interval (**Figure 2**). Fresh samples were handpicked for geochemical analyses. After cleaning in an ultrasonic bath, the samples were crushed using a tungsten carbide mortar and pestle then pulverized in an agate ball mill. The samples were heated at 550°C for 4 h and 950°C for 2 h to decompose organic matter and carbonate material respectively prior to analysis of major elements and loss on ignition was measured.

Major elements (SiO_2, TiO_2, Al_2O_3, Fe_2O_3, MnO, MgO, CaO, Na_2O, K_2O, and P_2O_5) were analyzed by X-ray fluorescence (ZSX Primus II, Rigaku Co., Japan) at Waseda University. To minimize matrix effects and mineral effects, the fused disk method was used with a sample to lithium borate flux ratio of 1:10. Calibration lines were created using reference samples GSJ (JDo-1, JSd-1, JSd-2, JSd-3, JSI-2, JLk-1, JCh-1, JA-2, JA-3, JB-1a, JB-2, JB-3, JG-1a, JG-2, JG-3, JGb-1, JP-1, JR-1, JR-2). The accuracy of calibration lines for all elements was better than 0.6%. The sample R39, which is located on *ca.* 60 cm below the bottom of CS-1, was hand-picked and measured twice because it showed very high CaO and P_2O_5 concentrations.

Some mudstone samples were observed using scanning electron microscopy (SEM-EDS, Hitachi S-3400N, Japan) at the Waseda University with an accelerating voltage of 15 kV. Soft X-ray photography was employed using a Naomi NX digital X-ray Transmission System (RF Co., Ltd, Japan) with tube voltage of 50 kV and tube current of 40 mA at the Waseda University.

3.2 Multivariate Statistics

3.2.1 Hierarchical Cluster Analysis

Q-mode cluster analysis was conducted to classify the compositional behavior of major elements. Variation matrix (Aitchison, 1986), which consists of variances of all possible

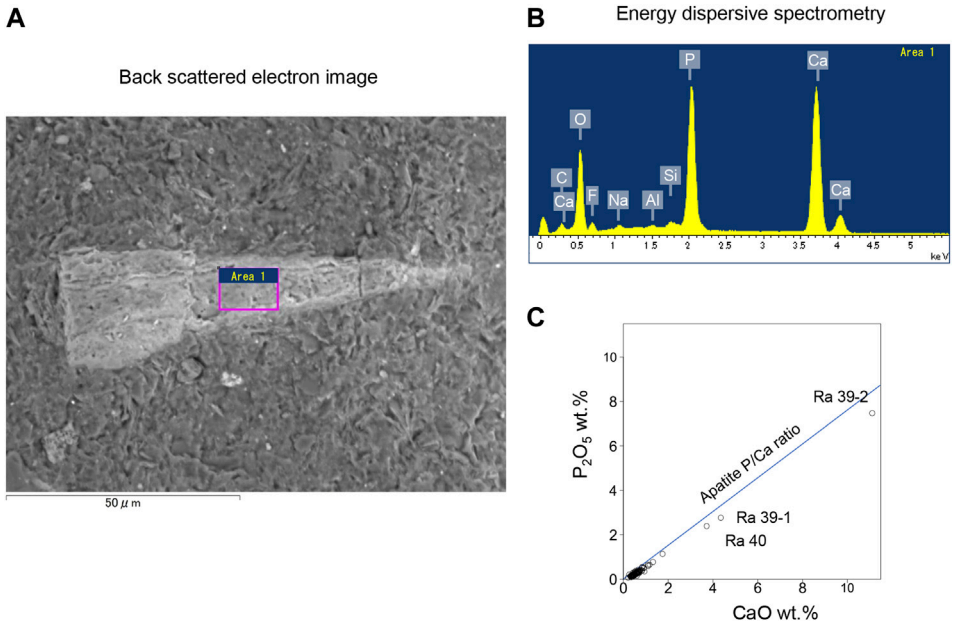

FIGURE 5 | (A) Scanning electron microscopy (SEM) image of the intercalated mudstone. Purple square indicates the region within an apatite for the Energy dispersive spectrometry (EDS) analysis. **(B)** Energy dispersive spectrometry of the apatite fragment. **(C)** Scatter plot of CaO and P_2O_5 of the whole-rack chemical compositions. The variation of the samples is along with the apatite P/Ca ratio.

logratios among components, was used as a distance matrix. Ward algorithm, which hierarchically groups the cluster by minimizing the total within-cluster variance, was used for the clustering criteria.

3.2.2 Principal Component Analysis

To investigate the latent variables that underlie the multivariate data, principal component analysis (PCA) was performed on the major element chemistry. PCA extracts the direction of maximum variance of the input dataset. Prior to PCA, the compositional data of 10 major elements are transformed to centered logratio (clr) space to avoid constant-sum constraint during the calculation without causing an increase in the dimension of the dataset (Aitchison, 1982; Ohta and Arai, 2007). The equation for clr transformation of major element compositional data $x = (SiO_2, TiO_2, \ldots, P_2O_5)$ is as follows:

$$\mathrm{clr}(x) = \left[\ln\frac{SiO_2}{(SiO_2 \times TiO_2 \times \cdots \times P_2O_5)^{1/10}}, \ln\frac{TiO_2}{(SiO_2 \times TiO_2 \times \cdots \times P_2O_5)^{1/10}}, , \cdots, \ln\frac{P_2O_5}{(SiO_2 \times TiO_2 \times \cdots \times P_2O_5)^{1/10}}\right]$$

To obtain robust results in the presence of outliers, robust PCA ('Hubert method', Hubert et al., 2005) were used for the current study. In the current dataset, some samples show a high abundance of specific elements (e.g., CaO, P_2O_5), indicating the anomalously high concentration of some mineral(s). Since PCA captures the direction of the highest variance of the given dataset, avoiding outliers before analysis is indispensable for investigating the latent variables, if any, of the structure of the dataset. The minimum covariance determinant method was adopted for outlier detection on the current dataset and the correlation matrix was used for the PCA calculation. Shapiro-Wilk test was used to evaluate normality of the clr variables after removing detected outliers.

The R package "compositions" (van den Boogaart and Tolosana-Delgado, 2008) and "rrcov" (Filzmoser and Todorov, 2013) were used for the cluster analysis and principal component analysis calculations.

4 RESULT

4.1 Major Element Geochemistry

The result of major element composition of the intercalated mudstone samples and data normalized by PAAS (Post Archean Australian Shale; Taylor and McLennan, 1985) are shown in **Table 1** and **Figure 4**, and **Supplementary Figure S1**. To avoid the false correlation effect of silica dilution, TiO_2 was used to normalize the major element concentrations. The elemental abundance of the intercalated mudstones relative to TiO_2 is generally similar to PAAS, except for CaO, Na_2O, MnO (**Figure 4**). The value of MnO/TiO_2 of the studied samples is higher than that of PAAS, whereas CaO/TiO_2 and Na_2O/TiO_2 are distinctively depleted.

The presence of apatite has a significant effect on the CaO and P_2O_5 concentration. **Figure 5** shows the Back Scatter Electron (BSE) image, Energy dispersive spectrometry, and scatter plot of CaO and P_2O_5 of the intercalated mudstones. Apatite fragments were observed in SEM. The concentration of CaO and P_2O_5 shows a clear positive correlation along with the

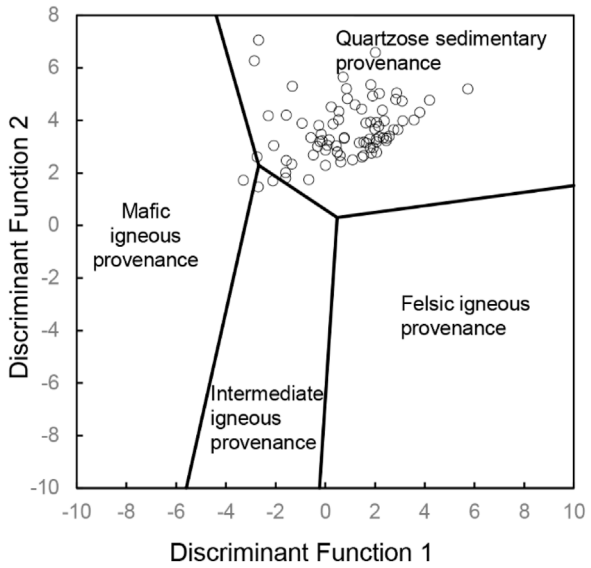

FIGURE 6 | Plot of the provenance discrimination diagram of Roser and Korsch (1988) for the studied mudstones. The Al-normalized version of the diagram of Roser and Korsch (1988) was adopted to avoid dilution effect of non-terrigenous materials. Samples are generally plotted within the "Quartzose sedimentary provenance" region, implying a source area of the intercalated mudstones located in a continental interior. Discriminant Function 1: 30.638×TiO2/Al2O3 – 12.541×Fe2O3/Al2O3 + 7.329×MgO/Al2O3 +12.031×Na2O/Al2O3 + 35.402×K2O/Al2O3 - 6.382. Discriminant Function 2: 56.500×TiO2/Al2O3 – 10.879×Fe2O3/Al2O3 + 30.875×MgO/Al2O3 – 5.404×Na2O/Al2O3 + 11.112×K2O/Al2O3 – 3.809.

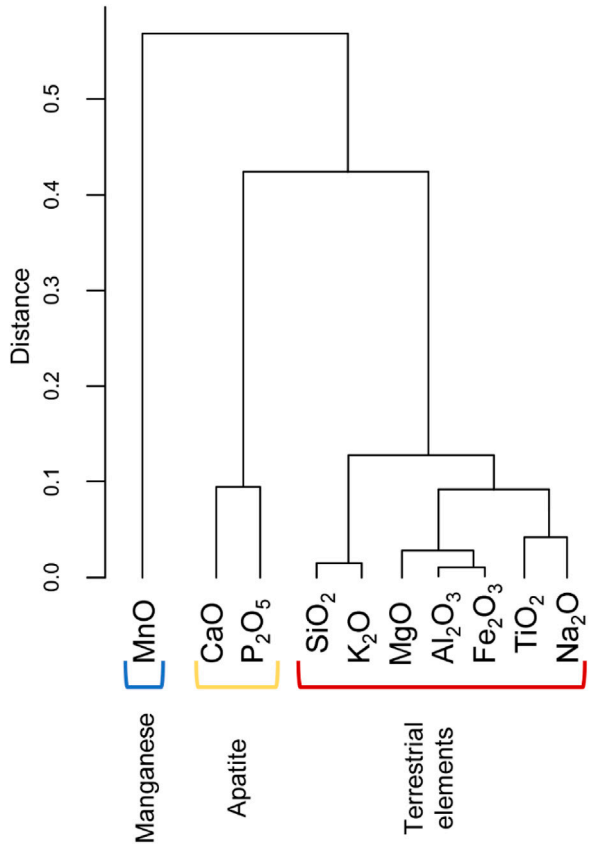

FIGURE 7 | Cluster analysis of the major element composition of intercalated mudstones in Section R and Section Q. Variation matrix (Aitchison, 1986) and Ward method was used for the distance. Three components that control the bulk chemical composition of the intercalated mudstone are classified ("manganese"; "apatite"; "terrestrial elements").

P_2O_5/CaO of 0.75, the ratio of apatite (e.g. Takiguchi et al., 2006).

To evaluate the possible provenance of the studied materials, provenance discrimination diagram of Roser and Korsch (1988) were adopted (**Figure 6**). Almost all samples are plotted in the "Quartzose sedimentary provenance".

To identify groups of elements with the same behavior, Q-mode cluster analysis were performed on the bulk chemical composition of the studied mudstones (**Figure 7**). Results of a cluster ordination of the different variables point to the different grouping of elements associated with siliciclastics (SiO_2, K_2O, MgO, Al_2O_3, Fe_2O_3, TiO_2, and Na_2O) and apatite elements (CaO and P_2O_5) along with MnO, which solely consists of a cluster.

4.2 Principal Component Analysis

To investigate latent information of the bulk chemical composition of the studied samples, PCA was performed (**Table 2**; **Figure 8**). The *p*-values of the Shapiro-Wilk test are 0.35 for clr (SiO_2), 0.44 for clr (TiO_2), 0.14 for clr (Al_2O_3), 0.45 for clr (Fe_2O_3), 0.86 for clr (MnO), 0.70 for clr (MgO), 0.09 for clr (CaO), 0.59 for clr (Na_2O), 0.04 for clr (K_2O), and 0.84 for clr (P_2O_5).

PC1 accounts for 38.9% of the variance of the clr-transformed dataset. PC1 has positive loading from Al_2O_3, K_2O, Na_2O, MgO, SiO_2, TiO_2, and Fe_2O_3, whereas it has negative loading from MnO, P_2O_5, and CaO. Elements positively loaded on PC1 belong to the siliciclastic cluster of above mentioned Q-mode cluster analysis. On the contrary, the elements belonging to the other two clusters (the cluster of manganese and apatite minerals) show negative loadings on PC1.

TABLE 2 | Results of principal component analysis.

	PC1	PC2	PC3	PC4
SiO_2	0.211	–0.200	0.289	–0.835
TiO_2	0.176	0.052	–0.634	–0.042
Al_2O_3	0.526	–0.040	0.091	0.207
Fe_2O_3	0.119	–0.364	–0.184	0.136
MnO	–0.305	–0.508	–0.221	0.028
MgO	0.315	-0.233	0.269	0.450
CaO	–0.179	0.396	0.226	0.095
Na_2O	0.333	0.420	–0.474	–0.143
K_2O	0.469	0.127	0.236	0.025
P_2O_5	–0.282	0.401	0.142	0.078
Eigen value	3.012	1.789	1.239	0.847
Variance explained	38.89	23.10	16.00	10.93
Cumulative variance	38.89	61.99	77.99	88.92

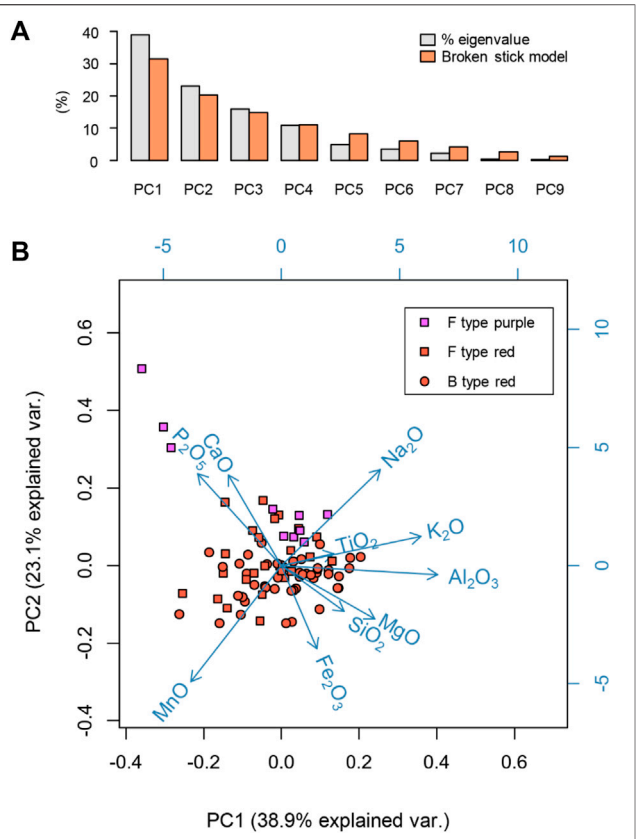

FIGURE 8 | (A) Scree plot of the PCA result and the Broken-Stick model (MacArthur, 1957) for the clr-transformed dataset of intercalated mudstones of Section R and Section Q. **(B)** Biplot of principal component scores and loadings for the PC1 and PC2.

Stratigraphic variations of PC1 and Al_2O_3/TiO_2 ratio are shown in **Figure 9**. The PC1 and Al_2O_3/TiO_2 show a weak positive correlation (R = 0.3). Al_2O_3/TiO_2 ratio increased across the CS-1, and then decreased across the B type/F type boundary but this trend is within the fluctuation throughout the studied section. The stratigraphic variation of PC1 along with the other elemental percent data is shown in **Supplementary Table S1**.

PC2, which is statistically orthogonal with PC1, accounts for 23.1% of the variance of the clr-transformed dataset. PC2 is characterized by high positive loading from P_2O_5, CaO, and Na_2O, and negative loading from MnO and Fe_2O_3.

5 DISCUSSION

5.1 Characterization of Intercalated Mudstone in the Bedded Cherts

The depositional site of the studied bedded chert is located on the deep-sea plane, which was isolated from continental fluvial transportation by trench (**Figure 1**; Matsuda and Isozaki, 1991). Thus, terrigenous materials contained by the bedded cherts are considered to supplied from aeolian transportation (Asahara, 1999). The provenance discrimination diagram of Roser and Korsch (1988) suggests that the provenance of the studied samples is from "Quartzose sedimentary provenance" (**Figure 6**). This result is concordant with the supposed transportation mode of the bedded cherts, that is, the terrigenous materials were blown in from continental interiors (Hori et al., 1993).

The major elemental compositions of the studied intercalated mudstone samples reflect the varying proportions of lithogenic, biogenic, and hydrogenic components in the sediments. The results of Q-mode cluster analysis point to the different grouping of "manganese" (Mn), "apatite" (Ca, P), and "terrestrial" elements (SiO_2, K_2O, MgO, Al_2O_3, Fe_2O_3, TiO_2, and Na_2O) (**Figure 7**).

Mn in our samples is enriched relative to PAAS (**Figure 4**). MnO along with Fe_2O_3 shows large negative loadings in PC2. Mn hydroxides or oxides (e.g., MnO_2) are deposited rapidly in particulate form under oxic conditions, whereas under suboxic and anoxic conditions Mn is reduced to divalent (Mn^{2+}) and forms soluble cations (Sholkovitz et al., 1992; Calvert and Pedersen, 1993). It is thus suggested that the enrichment of Mn may reflect an oxic depositional environment of this section. Alternatively, additional Mn may form under surface oxidized Mn-rich zones during diagenesis (e.g., Pedersen et al., 1986).

The variation of CaO and P_2O_5 in our dataset is controlled by apatite content because of the strong positive correlation of CaO and P_2O_5 with the P_2O_5/CaO ratio of 0.27–0.69 similar to apatite (**Figure 5**). Takiguchi et al. (2006) interpreted the main carrier of apatite in this succession was authigenic in origin and formed during early diagenesis based on their P_2O_5/CaO ratio lower than that of conodont apatite (~0.74; e.g., Ruttenberg and Berner, 1993; Van Cappellen and Berner, 1991). The variation of CaO, P2O5, and MnO characterize PC2, which contains 23.1% of the total variance of the studied dataset. CaO and P_2O_5 show large positive loading whereas MnO shows negative loading, indicating the opposite influence of phosphate and manganese. This relation agrees with the chemistry variation under manganese redirection (Dickens and Owen, 1994; Betzler et al., 2016; Bialik et al., 2020).

The total concentrations of "manganese" and "apatite" elements are generally less than 5%, except for the extremely low PC1 samples at *ca.* 20 cm below the thick claystone CS-1 (Sample Ra39-1, Ra39-2, Ra40). These levels correspond to the unusually high values of CaO and P_2O_5 contents with "apatite" elements content of ca. 7–18%, which can be recognized as an event bed (**Figure 5** and **Figure 9**). The P_2O_5/CaO ratio of these three samples are within 0.6–0.7, lower than that of conodont apatite (Takiguchi et al., 2006). This unusually high apatite concentration may be caused by a pelagic marine environmental shift which led to precipitate abiotic apatite in the sediments, but this topic remains outside the scope of this paper.

For "terrestrial" elements, although biogenic Si is the main component of radiolarian chert, Si in intercalated mudstone is considered to be mainly derived from siliciclastic materials due to migration of biogenic silica to adjacent chert during diagenesis segregation (e.g., Tada, 1991). During this diagenetic segregation,

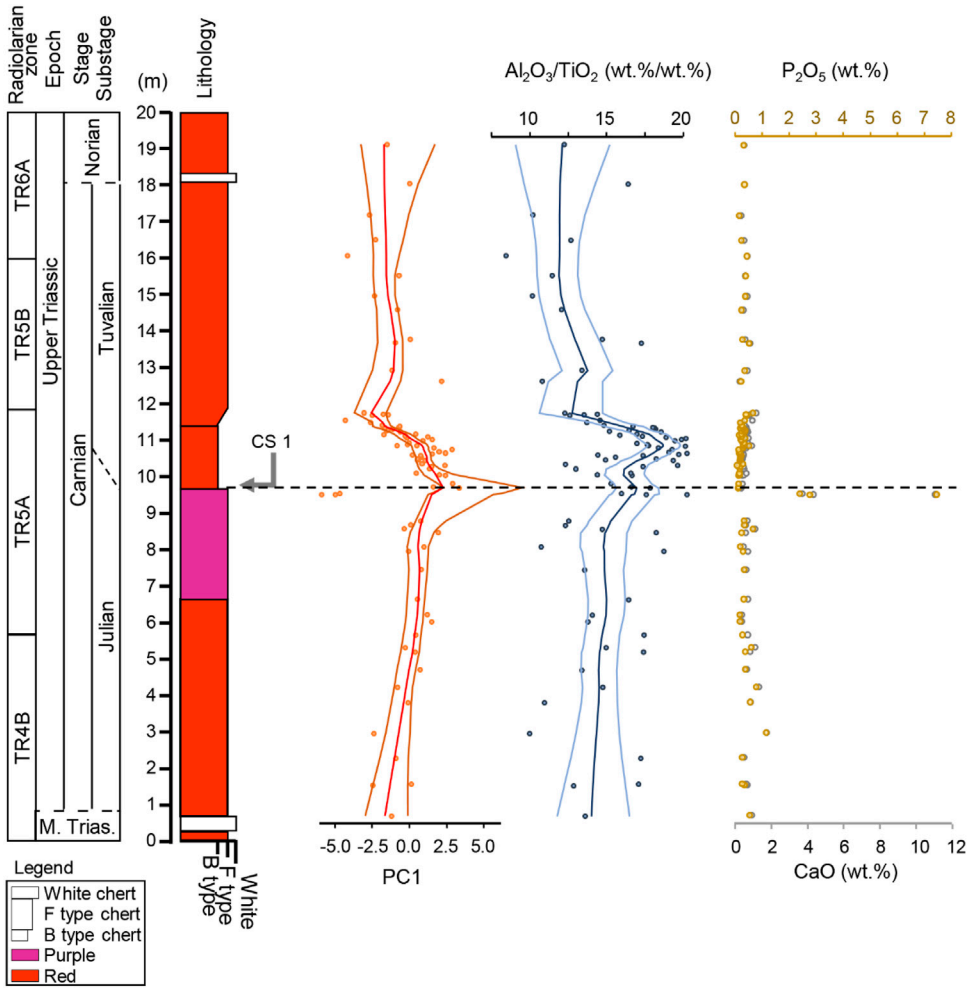

FIGURE 9 | The stratigraphic profile of principal component 1 (PC1) scores and Al_2O_3/TiO_2 ratios. Lines indicate LOWESS fitting and 95% confidence intervals. The relatively high PC1 interval (*ca*. 1 m thick) can be seen above the CS-1. The outstandingly low PC1 observed just below the CS1 corresponds to the high CaO and P_2O_5 samples (Ra39-1, Ra39-2, Ra40).

opal-A in siliceous fossils are extensively dissolved and reprecipitated as tiny opal-CT particles within the pore space mainly in higher dissolved Si area, and thus Si migrated from proto-mudstone intervals to adjacent proto-chert intervals (e.g., Tada, 1991). We cannot rule out contamination of biogenic Si in the intercalated mudstones, but the contribution should be negligible because only well-sorted mudstones were selected for the geochemical analysis.

5.2 Reconstruction of Terrigenous Fluctuations to the Panthalassa Superocean Through the Carnian

PC1 gradually increases below CS-1 from -1.5 to 1, except for the extremely negative values *ca.* 20 cm below the CS-1 (Sample Ra39-1, Ra39-2, Ra40). The PC1 score suddenly increases to 3.4 at the CS-1 horizon and remains constantly high values around 1.5 at the following *ca*. 1 m thick B-type bedded chert interval. The PC1 values decrease across the B type and F type boundary, and then seem to maintain a steady-state with higher variations than Julian to the end of Tuvalian.

Since PC1 has positive loading on all the "terrestrial" elements and negative loading on "manganese" and "apatite" elements, PC1 can be regarded as a latent variable that denotes the degree of relative contribution of terrigenous materials against marine-derived components. Besides, PC1 scores do not show a negative correlation with Al_2O_3/TiO_2 ratio ($R = 0.3$). Al_2O_3/TiO_2 ratio is known to reflect biological productivity on the abyssal fine-grained marine sediments since excess Al is scavenged by the biological pump (Murray and Leinen, 1996; Dymond et al., 1997). The studied bedded cherts are estimated to be deposited at the low latitude of abyssal deep-sea Panthalassa (Ando et al., 2001; Uno et al., 2015) thus the fluctuation of Al_2O_3/TiO_2 ratio of the

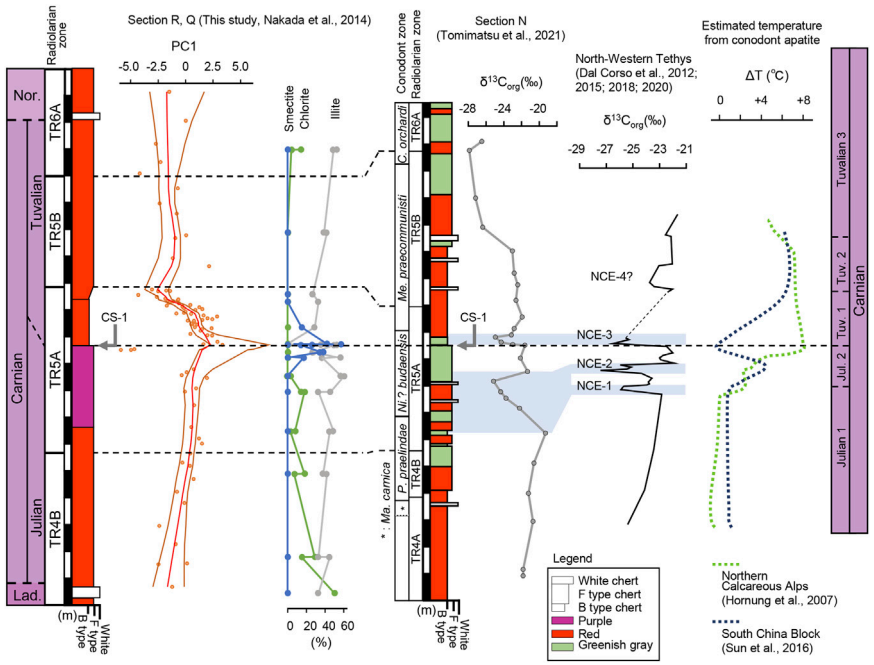

FIGURE 10 | The comparison of PC1 with compositional variation of Fe-bearing minerals and paleotemperature across the CPE. The occurrence of smectite (Nakada et al., 2014) overlaps with the high PC1 interval. Section R and Section N of Inuyama area are correlated by radiolarian biozone and CS-1 as a key bed (Sugiyama, 1997). The conodont and carbon isotope correlations are based on Dal Corso et al. (2020) and Tomimatsu et al. (2021). Paleotemperature profiles are calculated from oxygen isotope of conodont apatite from the western Tethys and the South China Block (Hornung et al., 2007; Sun et al., 2016; redrawn from; Dal Corso et al., 2018).

current dataset is expected to reflect productivity. Therefore, the non-negative correlation observed between PC1 and Al_2O_3/TiO_2 suggests that the changes in PC1 are not mainly regulated by biological productivity fluctuations.

In addition, lithology of the bedded chert suddenly changes from F-type to B-type just above CS-1, with corresponding increased mudstone thickness (Sugiyama, 1997) and an increase in PC1 (**Figure 9**). Two possible factors that regulate the type of bedded chert (F type or B type) that is, the changes in burial flux of biogenic silica and/or siliciclastics (Sugiyama, 1997). Because of the increased Al_2O_3/TiO_2 ratio across the CS-1, a coincident increase in PC1 score may reflect increased terrigenous supply rather than decreased productivity (**Figure 9**).

Equally, considering the negligible contribution of "manganese" and "apatite" elements in samples other than Ra39 and Ra40, the increased mudstone bed thickness across CS-1 likely reflects increased flux of terrigenous material, probably eolian dust in the equatorial pelagic Panthalassa (Hori et al., 1993).

5.3 Continental Environmental Condition Inferred by Terrigenous Supply and Clay Mineral Content Fluctuations of Deep-Sea Bedded Chert

The Carnian Pluvial Episode has been characterized by abrupt siliciclastic input in Tethyan regions (Schlager and Schollnberger, 1974; Simms and Ruffell, 1989; Simms and Ruffell, 1990). This study suggests an increased terrigenous input also occurred in the abyssal deep-sea Panthalassa across the CPE. The increases in siliciclastic input at continental and coastal regions are considered to have been a consequence of enhanced hydrological cycling and consequent increased runoff. However, as discussed above, the terrigenous input in the abyssal plane reflects increasing eolian supply (Hori et al., 1993). Since this eolian dust is likely blown from arid continental areas, the increasing terrigenous supply detected in this study may imply the extensive aridification of the Pangean supercontinent.

This idea seems to contradict the existence of smectite across the CPE which was interpreted as evidence of continental humidification (Nakada et al., 2014). However, a megamonsoonal climate was known to prevail during the Triassic owing to the configuration of supercontinent-superocean (e.g., Kutzbach and Gallimore, 1989). Observational and climate modeling studies at the present day have indicated the humidification of tropical regions and aridification of subtropical regions under global warming (i.e., "Dry gets drier, wet gets wetter"; Held and Soden, 2006). The expansion of arid regions and associated aridification of previously humid regions could account for production of eolian dust containing smectite. The arid and seasonal influences around Carnian are detected in some Gondwana successions (Ruffell et al., 2016).

Expansion of arid regions could have also increased the emission of eolian dust with smectite across CS-1. Eolian

deposits temporarily appeared in the Fundy (Canada), Iberian (Spain) and Argana (Morocco) basins during the Carnian, possibly near the end of the CPE, based on the limited biostratigraphy of terrestrial vertebrates and plant fossils (Arche and López-Gómez, 2014; Sues and Olsen, 2015). Interestingly, the onset of the smectite-rich interval slightly preceded the increased mudstone bed thickness across the CS-1 (**Figure 10**; Sugiyama, 1997; Sugiyama et al., 2001; Nakada et al., 2014). This temporal relation is consistent with the formation of smectite during the CPE and subsequent increase in eolian dust flux owing to the expansion of arid regions in the previously humid regions. Besides, weathering of mafic volcanic sources could also account for the smectite.

Increasing wind gustiness by global cooling and increased latitudinal temperature difference is also known as a main cause of increased eolian flux increase on glacial-interglacial timescales (e.g., McGee et al., 2010). Across the CPE, high-resolution sea surface temperature profile derived from oxygen-isotope of conodont apatite show a possible two-pulse warming event in the Nanpanjiang Basin in South China Block (Sun et al., 2016), while other low-resolution records from western Tethys show only one pulse (e.g., Hornung et al., 2007). In the South China Block, the onset of the CPE, namely NCIE-1, coincided with the first pulse of warming of ~4°C, and followed by a short cooling phase across the Julian/Tuvalian boundary, and then by a prolonged and more intense second phase of warming (**Figure 10**; Sun et al., 2016). According to the biostratigraphy and carbon isotope correlation (**Figure 10**; Tomimatsu et al., 2021), the CS-1 level can be correlated with this short cooling phase across the Julian/Tuvalian boundary. Thus, cooling and associated wind gustiness, in addition to the expansion of arid regions, could have also enhanced the eolian dust emission recorded as the lithologic change in this study section (Sugiyama, 1997).

6 CONCLUSION

The cluster analysis and principal component analysis for the major element composition of intercalated mudstone within bedded chert were performed to investigate the continental environment fluctuation in the Carnian. The PC1 represents the terrigenous content fluctuation whereas PC2 reflects the relative contribution of manganese over apatite. The stratigraphic variation of PC1, coupled with an increase in mudstone thickness, suggests that terrigenous content in abyssal deep-sea sediments from Japan increased at around the Julian/Tuvalian boundary (i.e., across the CPE), and then return to pre-CPE level in Tuvalian. A delayed increase in dust flux relative to an increase in smectite content in deep-sea chert implied expansion of arid regions and associated aridification of previously humid regions. The appearance of eolian successions in low-latitude Pangea are consistent with this idea, but these age models have large uncertainty. This study thus provides deep-sea evidence for widespread aridification that occurred in the Pangean interior across the Julian/Tuvalian boundary, potentially related to CPE.

In addition, an event bed with very high apatite content was found immediately before the high terrigenous supply interval, implying environmental perturbation occurred in pelagic Panthalassa, potentially related to the CPE.

DATA AVAILABILITY STATEMENT

The original contributions presented in the study are included in the article/**Supplementary Material**, further inquiries can be directed to the corresponding author.

AUTHOR CONTRIBUTIONS

TC, MI, and TO contributed to the design and implementation of the research, to the fieldwork, to the analysis of the results and to the writing of the manuscript.

FUNDING

This project was financially supported by Japan Society for the Promotion of Science (21J10870), Fukada geological institute (Grant-in-Aid for feildwork), Waseda Research Institute for Science and Engineering (Grant-in-Aid for Young Scientists: Early-Bird; BD070Z003800).

ACKNOWLEDGMENTS

Thanks go to Yoshiaki Suzuki, Arisa Nakano, Shun Ebisawa and Taro Higuchi for help in the fieldwork, laboratory work, and fruitful discussions. We are grateful to David B. Kemp for fruitful comments, which greatly enhanced the quality of this work. We also thank two reviewers for their helpful and thoughtful reviews.

SUPPLEMENTARY MATERIAL

The Supplementary Material for this article can be found online at: https://www.frontiersin.org/articles/10.3389/feart.2022.897396/full#supplementary-material

REFERENCES

Aitchison, J. (1982). The Statistical Analysis of Compositional Data. *J. R. Stat. Soc. Ser. B Methodol.* 44, 139–160. doi:10.1111/j.2517-6161.1982.tb01195.x

Aitchison, J. (1986). *The Statistical Analysis of Compositional Data/J. Aitchison*. London: Chapman & Hall.

Ando, A., Kodama, K., and Kojima, S. (2001). Low-latitude and Southern Hemisphere Origin of Anisian (Triassic) Bedded Chert in the Inuyama Area, Mino Terrane, Central Japan. *J. Geophys. Res.* 106, 1973–1986. doi:10.1029/2000jb900305

Arche, A., and López-Gómez, J. (2014). The Carnian Pluvial Event in Western Europe: New Data from Iberia and Correlation with the Western Neotethys and Eastern North America-NW Africa Regions. *Earth-Science Rev.* 128, 196–231. doi:10.1016/j.earscirev.2013.10.012

Asahara, Y. (1999). 87Sr/86Sr Variation in North Pacific Sediments: a Record of the Milankovitch Cycle in the Past 3 Million Years. *Earth Planet. Sci. Lett.* 171, 453–464. doi:10.1016/s0012-821x(99)00158-2

Baranyi, V., Miller, C. S., Ruffell, A., Hounslow, M. W., and Kürschner, W. M. (2019a). A Continental Record of the Carnian Pluvial Episode (CPE) from the Mercia Mudstone Group (UK): Palynology and Climatic Implications. *J. Geol. Soc.* 176, 149–166. doi:10.1144/jgs2017-150

Baranyi, V., Rostási, Á., Raucsik, B., and Kürschner, W. M. (2019b). Palynology and Weathering Proxies Reveal Climatic Fluctuations during the Carnian Pluvial Episode (CPE) (Late Triassic) from Marine Successions in the Transdanubian Range (Western Hungary). *Glob. Planet. Change* 177, 157–172. doi:10.1016/j.gloplacha.2019.01.018

Barrenechea, J. F., López-Gómez, J., and De La Horra, R. (2018). Sedimentology, Clay Mineralogy and Palaeosols of the Mid-carnian Pluvial Episode in Eastern Spain: Insights into Humidity and Sea-Level Variations. *J. Geol. Soc.* 175, 993–1003. doi:10.1144/jgs2018-024

Bernardi, M., Gianolla, P., Petti, F. M., Mietto, P., and Benton, M. J. (2018). Dinosaur Diversification Linked with the Carnian Pluvial Episode. *Nat. Commun.* 9, 1499. doi:10.1038/s41467-018-03996-1

Betzler, C., Eberli, G. P., Kroon, D., Wright, J. D., Swart, P. K., Nath, B. N., et al. (2016). The Abrupt Onset of the Modern South Asian Monsoon Winds. *Sci. Rep.* 6, 29838. doi:10.1038/srep29838

Bialik, O. M., Reolid, J., Betzler, C., Eberli, G. P., and Waldmann, N. D. (2020). Source Shifts to Periplatform Deposits during the Early to Middle Miocene in Response to Climatic and Oceanographic Forcing, Maldives, Western Indian Ocean. *Palaeogeogr. Palaeoclimatol. Palaeoecol.* 559, 109969. doi:10.1016/j.palaeo.2020.109969

Calvert, S. E., and Pedersen, T. F. (1993). Geochemistry of Recent Oxic and Anoxic Marine Sediments: Implications for the Geological Record. *Mar. Geol.* 113, 67–88. doi:10.1016/0025-3227(93)90150-t

Cappellen, P. V., and Berner, R. A. (1991). Fluorapatite Crystal Growth from Modified Seawater Solutions. *Geochimica Cosmochimica Acta* 55, 1219–1234. doi:10.1016/0016-7037(91)90302-l

Dal Corso, J., Mietto, P., Newton, R. J., Pancost, R. D., Preto, N., Roghi, G., et al. (2012). Discovery of a Major Negative 13C Spike in the Carnian (Late Triassic) Linked to the Eruption of Wrangellia Flood Basalts. *Geology* 40, 79–82. doi:10.1130/g32473.1

Dal Corso, J., Gianolla, P., Newton, R. J., Franceschi, M., Roghi, G., Caggiati, M., et al. (2015). Carbon Isotope Records Reveal Synchronicity between Carbon Cycle Perturbation and the "Carnian Pluvial Event" in the Tethys Realm (Late Triassic). *Glob. Planet. Change* 127, 79–90. doi:10.1016/j.gloplacha.2015.01.013

Dal Corso, J., Gianolla, P., Rigo, M., Franceschi, M., Roghi, G., Mietto, P., et al. (2018). Multiple Negative Carbon-Isotope Excursions during the Carnian Pluvial Episode (Late Triassic). *Earth-science Rev.* 185, 732–750. doi:10.1016/j.earscirev.2018.07.004

Dal Corso, J., Bernardi, M., Sun, Y., Song, H., Seyfullah, L. J., Preto, N., et al. (2020). Extinction and Dawn of the Modern World in the Carnian (Late Triassic). *Sci. Adv.* 6, eaba0099. doi:10.1126/sciadv.aba0099

Dickens, G. R., and Owen, R. M. (1994). Late Miocene-Early Pliocene Manganese Redirection in the Central Indian Ocean: Expansion of the Intermediate Water Oxygen Minimum Zone. *Paleoceanography* 9, 169–181. doi:10.1029/93pa02699

Dymond, J., Collier, R., McManus, J., Honjo, S., and Manganini, S. (1997). Can the Aluminum and Titanium Contents of Ocean Sediments Be Used to Determine the Paleoproductivity of the Oceans? *Paleoceanography* 12, 586–593. doi:10.1029/97pa01135

Filzmoser, P., and Todorov, V. (2013). Robust Tools for the Imperfect World. *Inf. Sci.* 245, 4–20. doi:10.1016/j.ins.2012.10.017

Gattolin, G., Preto, N., Breda, A., Franceschi, M., Isotton, M., and Gianolla, P. (2015). Sequence Stratigraphy after the Demise of a High-Relief Carbonate Platform (Carnian of the Dolomites): Sea-Level and Climate Disentangled. *Palaeogeogr. Palaeoclimatol. Palaeoecol.* 423, 1–17. doi:10.1016/j.palaeo.2015.01.017

Held, I. M., and Soden, B. J. (2006). Robust Responses of the Hydrological Cycle to Global Warming. *J. Clim.* 19, 5686–5699. doi:10.1175/jcli3990.1

Hori, R. S., Cho, C.-F., and Umeda, H. (1993). Origin of Cyclicity in Triassic-Jurassic Radiolarian Bedded Cherts of the Mino Accretionary Complex from Japan. *Isl. Arc* 2, 170–180. doi:10.1111/j.1440-1738.1993.tb00084.x

Hori, S. R., Higuchi, Y., and Fujiki, T. (2000). Chemical Composition and Their Environmental Records of Bedded Cherts from Accretionary Complexes in Japan. *Mem. Geol. Soc. Jpn.* 55, 43–59. (in Japanese).

Hornung, T., Brandner, R., Krystyn, L., Joachimski, M. M., and Keim, L. (2007). Multistratigraphic Constraints on the NW Tethyan "Carnian Crisis". *Glob. Triassic* 41, 59–67.

Hubert, M., Rousseeuw, P. J., and Vanden Branden, K. (2005). ROBPCA: a New Approach to Robust Principal Component Analysis. *Technometrics* 47, 64–79. doi:10.1198/004017004000000563

Ikeda, M., and Tada, R. (2014). A 70 Million Year Astronomical Time Scale for the Deep-Sea Bedded Chert Sequence (Inuyama, Japan): Implications for Triassic-Jurassic Geochronology. *Earth Planet. Sci. Lett.* 399, 30–43. doi:10.1016/j.epsl.2014.04.031

Imoto, N. (1983). "Chapter 22 Sedimentary Structures of Permian-Triassic Cherts in the Tamba District, Southwest Japan," in *Anonymous Developments in Sedimentology* (Elsevier), 377–393. doi:10.1016/s0070-4571(08)70101-8

Kimura, K., and Hori, R. (1993). Offscraping Accretion of Jurassic Chert-Clastic Complexes in the Mino-Tamba Belt, Central Japan. *J. Struct. Geol.* 15, 145–161. doi:10.1016/0191-8141(93)90092-o

Kutzbach, J. E., and Gallimore, R. G. (1989). Pangaean Climates: Megamonsoons of the Megacontinent. *J. Geophys. Res.* 94, 3341–3357. doi:10.1029/jd094id03p03341

Lindström, S., Erlström, M., Piasecki, S., Nielsen, L. H., and Mathiesen, A. (2017). Palynology and Terrestrial Ecosystem Change of the Middle Triassic to Lowermost Jurassic Succession of the Eastern Danish Basin. *Rev. Palaeobot. Palynol.* 244, 65–95. doi:10.1016/j.revpalbo.2017.04.007

Lu, J., Zhang, P., Dal Corso, J., Yang, M., Wignall, P. B., Greene, S. E., et al. (2021). Volcanically Driven Lacustrine Ecosystem Changes during the Carnian Pluvial Episode (Late Triassic). *Proc. Natl. Acad. Sci. U. S. A.* 118, 5118. doi:10.1073/pnas.2109895118

MacArthur, R. H. (1957). On the Relative Abundance of Bird Species. *Proc. Natl. Acad. Sci. U.S.A.* 43, 293–295. doi:10.1073/pnas.43.3.293

Matsuda, T., and Isozaki, Y. (1991). Well-documented Travel History of Mesozoic Pelagic Chert in Japan: From Remote Ocean to Subduction Zone. *Tectonics* 10, 475–499. doi:10.1029/90tc02134

Matthews, K. J., Maloney, K. T., Zahirovic, S., Williams, S. E., Seton, M., and Müller, R. D. (2016). Global Plate Boundary Evolution and Kinematics since the Late Paleozoic. *Glob. Planet. Change* 146, 226–250. doi:10.1016/j.gloplacha.2016.10.002

McGee, D., Broecker, W. S., and Winckler, G. (2010). Gustiness: The Driver of Glacial Dustiness? *Quat. Sci. Rev.* 29, 2340–2350. doi:10.1016/j.quascirev.2010.06.009

Mueller, S., Hounslow, M. W., and Kürschner, W. M. (2016). Integrated Stratigraphy and Palaeoclimate History of the Carnian Pluvial Event in the Boreal Realm; New Data from the Upper Triassic Kapp Toscana Group in Central Spitsbergen (Norway). *J. Geol. Soc.* 173, 186–202. doi:10.1144/jgs2015-028

Murray, R. W., and Leinen, M. (1996). Scavenged Excess Aluminum and its Relationship to Bulk Titanium in Biogenic Sediment from the Central Equatorial Pacific Ocean. *Geochimica Cosmochimica Acta* 60, 3869–3878. doi:10.1016/0016-7037(96)00236-0

Nakada, R., Ogawa, K., Suzuki, N., Takahashi, S., and Takahashi, Y. (2014). Late Triassic Compositional Changes of Aeolian Dusts in the Pelagic Panthalassa: Response to the Continental Climatic Change. *Palaeogeogr. Palaeoclimatol. Palaeoecol.* 393, 61–75. doi:10.1016/j.palaeo.2013.10.014

Oda, H., and Suzuki, H. (2000). Paleomagnetism of Triassic and Jurassic Red Bedded Chert of the Inuyama Area, Central Japan. *J. Geophys. Res.* 105, 25743–25767. doi:10.1029/2000jb900267

Ohta, T., and Arai, H. (2007). Statistical Empirical Index of Chemical Weathering in Igneous Rocks: A New Tool for Evaluating the Degree of Weathering. *Chem. Geol.* 240, 280–297. doi:10.1016/j.chemgeo.2007.02.017

Pedersen, T. F., Vogel, J. S., and Southon, J. R. (1986). Copper and Manganese in Hemipelagic Sediments at 21 °N, East Pacific Rise: Diagenetic Contrasts. *Geochimica Cosmochimica Acta* 50, 2019–2031. doi:10.1016/0016-7037(86)90256-5

Roser, B. P., and Korsch, R. J. (1988). Provenance Signatures of Sandstone-Mudstone Suites Determined Using Discriminant Function Analysis of Major-Element Data. *Chem. Geol.* 67, 119–139. doi:10.1016/0009-2541(88)90010-1

Ruffell, A., Simms, M. J., and Wignall, P. B. (2016). The Carnian Humid Episode of the Late Triassic: a Review. *Geol. Mag.* 153, 271–284. doi:10.1017/s0016756815000424

Ruttenberg, K. C., and Berner, R. A. (1993). Authigenic Apatite Formation and Burial in Sediments from Non-upwelling, Continental Margin Environments. *Geochimica Cosmochimica Acta* 57, 991–1007. doi:10.1016/0016-7037(93)90035-u

Schlager, W., and Schöllnberger, W. (1974). Das Prinzip stratigraphischer Wenden in der Schichtfolge der Nördlichen Kalkalpen. *Mitt. Geol. Ges. Wien*. 66, 165–193.

Scotese, C. R. (2014). Atlas of Middle & Late Permian and Triassic Paleogeographic Maps. *Paleomap Proj.* 3, 49. doi:10.13140/2.1.2609.9209

Sholkovitz, E. R., Shaw, T. J., and Schneider, D. L. (1992). The Geochemistry of Rare Earth Elements in the Seasonally Anoxic Water Column and Porewaters of Chesapeake Bay. *Geochimica Cosmochimica Acta* 56, 3389–3402. doi:10.1016/0016-7037(92)90386-w

Simms, M. J., and Ruffell, A. H. (1989). Synchroneity of Climatic Change and Extinctions in the Late Triassic. *Geol* 17, 265–268. doi:10.1130/0091-7613(1989)017<0265:soccae>2.3.co;2

Simms, M. J., and Ruffell, A. H. (1990). Climatic and Biotic Change in the Late Triassic. *J. Geol. Soc.* 147, 321–327. doi:10.1144/gsjgs.147.2.0321

Sues, H., and Olsen, P. (2015). Stratigraphic and Temporal Context and Faunal Diversity of Permian-Jurassic Continental Tetrapod Assemblages from the Fundy Rift Basin, Eastern Canada. *Atl. Geol.* 51, 139–205.

Sugiyama, K., Kawakami, S., and Takano, M. (2001). *Aerial Photograph and Stratigraphic Correlation of the Triassic to Lower Jurassic Siliceous Claystone and Bedded Chert Units of the Inuyama and Hisuikyo Areas, Central Japan*. Osaka, Japan: News of Osaka Micropaleontologists, 145–157.

Sugiyama, K. (1997). Triassic and Lower Jurassic Radiolarian Biostratigraphy in the Siliceous Claystone and Bedded Chert Units of the Southeastern Mino Terrane, Central Japan. *Bull. Mizunami Fossil Mus.* 24, 79–193.

Sun, Y. D., Wignall, P. B., Joachimski, M. M., Bond, D. P. G., Grasby, S. E., Lai, X. L., et al. (2016). Climate Warming, Euxinia and Carbon Isotope Perturbations during the Carnian (Triassic) Crisis in South China. *Earth Planet. Sci. Lett.* 444, 88–100. doi:10.1016/j.epsl.2016.03.037

Tada, R. (1991). in *Compaction and Cementation in Siliceous Rocks and Their Possible Effect on Bedding Enhancement. Cycles and Events in Stratigraphy*. Editor G. Einsele, et al. (New York: Springer-Verlag), 480–491.

Takiguchi, T., Sugitani, K., Yamamoto, K., and Suzuki, K. (2006). Biogeochemical Signatures Preserved in Ancient Siliceous Sediments; New Perspectives to Triassic Radiolarian Bedded Chert Compositions. *Geochem. J.* 40, 33–45. doi:10.2343/geochemj.40.33

Taylor, S. R., and McLennan, S. M. (1985). *The Continental Crust: Its Composition and Evolution*. Oxford: Blackwellk, 312.

Tomimatsu, Y., Nozaki, T., Sato, H., Takaya, Y., Kimura, J.-I., Chang, Q., et al. (2021). Marine Osmium Isotope Record during the Carnian "Pluvial Episode" (Late Triassic) in the Pelagic Panthalassa Ocean. *Glob. Planet. Change* 197, 103387. doi:10.1016/j.gloplacha.2020.103387

Uno, K., Yamashita, D., Onoue, T., and Uehara, D. (2015). Paleomagnetism of Triassic Bedded Chert from Japan for Determining the Age of an Impact Ejecta Layer Deposited on Peri-Equatorial Latitudes of the Paleo-Pacific Ocean: A Preliminary Analysis. *Phys. Earth Planet. Interiors* 249, 59–67. doi:10.1016/j.pepi.2015.10.004

Van den Boogaart, K. G., and Tolosana-Delgado, R. (2008). "compositions": A Unified R Package to Analyze Compositional Data. *Comput. Geosciences* 34, 320–338. doi:10.1016/j.cageo.2006.11.017

Visscher, H., Van Houte, M., Brugman, W. A., and Poort, R. J. (1994). Rejection of a Carnian (Late Triassic) "Pluvial Event" in Europe. *Rev. Palaeobot. Palynology* 83, 217–226. doi:10.1016/0034-6667(94)90070-1

Yamashita, D., Kato, H., Onoue, T., and Suzuki, N. (2018). Integrated Upper Triassic Conodont and Radiolarian Biostratigraphies of the Panthalassa Ocean. *Paleontological Res.* 22, 167–197. doi:10.2517/2017pr020

Yao, A., Mtsuda, T., and Isozaki, Y. (1980). *Triassic and Jurassic Radiolarians from the Inuyama Area, Central Japan*. Osaka, Japan: Journal of Geosciences Osaka City University, 135–154.

Conflict of Interest: The authors declare that the research was conducted in the absence of any commercial or financial relationships that could be construed as a potential conflict of interest.

Publisher's Note: All claims expressed in this article are solely those of the authors and do not necessarily represent those of their affiliated organizations, or those of the publisher, the editors and the reviewers. Any product that may be evaluated in this article, or claim that may be made by its manufacturer, is not guaranteed or endorsed by the publisher.